PAPER

Check for updates

Impact of LiPON incorporation on the ionic conductivity of mixed oxy-sulfide glassy solid electrolytes†

Victor Torres, III, [ID] Steven Kmiec, Christopher Martin, Presley Phillip and Steve W. Martin [ID] *

Solid-state electrolytes (SSEs) with high ionic conductivity, stability, mechanical strength, and low cost are crucial for next-generation all-solid-state lithium batteries (ASSLBs). These materials could provide better safety, energy density, and lifespan than conventional lithium-ion batteries with liquid electrolytes. Some lithium glassy solid electrolytes (GSEs) stand out for their high ionic conductivity, wide electrochemical stability, and good compatibility with lithium metal anodes. Alkali oxide GSEs offer good chemical stability but suffer from very low ionic conductivity, whereas alkali sulfide GSEs provide much higher conductivity but are unstable with both low-reduction-potential lithium metal and high-oxidation-potential cathodes. Mixed oxy-sulfide (MOS) GSEs combine the benefits of oxides and sulfides, and incorporating nitrogen further enhances their properties, making mixed-oxy-sulfide-nitride GSEs promising candidates for ASSLBs. This study of $Li_2S + SiS_2 + LiPO_3 + LiPON$ mixed glass former MOSN GSEs investigates the influence of LiPON incorporation on the physical properties, electrochemical behavior, and ionic conductivity of the base MOS GSEs. The Christensen–Martin–Anderson–Stuart (CMAS) model was used to model the Li^+ ionic conductivity activation energy in terms of the coulombic binding and volumetric strain energy components. The binding energy for these GSEs was calculated as a function of the composition and found to be correlated with the concentration of di-coordinated nitrogen in the glass. Further, this study explored the structural, physical, and electrochemical properties of these GSEs and the impact of nitrogen incorporation on density, mechanical moduli, electrochemical stability, and dielectric permittivity. It was observed that the added nitrogen increased the ionic conductivity of these GSEs to 1.1 mS cm^{-1} at 25 °C and that the addition of nitrogen further improved electrochemical behavior when in contact with lithium metal. These results further show the advantageous role that added nitrogen can have upon the electrochemical properties of GSEs.

1. Introduction

High-performance solid-state electrolytes (SSE) are essential in advancing next-generation all-solid-state lithium batteries (ASSLBs) for electric vehicles and portable electronics.[1] Although lithium-ion batteries (LIBs) with organic liquid

Department of Materials Science and Engineering, Iowa State University of Science and Technology, 2240 Hoover Hall, 528 Bissell Rd, Ames, IA 50011, USA. E-mail: swmartin@iastate.edu

electrolytes (OLEs) have been the predominant commercially available batteries, LIBs are prone to thermal runaway and dendrite growth, leading to combustion and explosion.[2–4] The advancement of high-performance ASSLBs depends upon developing new electrolytes to achieve improved safety, energy density, and longevity compared to their liquid electrolyte based counterparts.[5–7] If achieved, these SSEs promise to revolutionize the battery industry. As such, their development is crucial to overcoming the limitations of current LIBs and meeting the growing demands of advanced electronic devices, electric vehicles, and renewable energy harvesters.[8,9]

Among the various types of SSEs, inorganic SSEs have become a promising candidate for ASSLBs.[10,11] In particular, lithium glassy solid electrolytes (GSEs) have attracted significant attention due to their favorable properties, including synthesis at temperatures below 1000 °C, broad electrochemical stability, and improved stability with lithium metal anodes.[12,13] Furthermore, the investigation and reports of inorganic GSEs that are homogenous, grain boundary-free, and inhibit dendrite

growth are becoming more frequent in the literature.[14–17] By exploring the various types of GSEs, a chemistry that meets the desired electrochemical needs for ASSLBs can be selected. The primary purpose if this work here is to optimize a GSE composition with tunable chemistries, excellent electrochemical properties, dry-room air stability, and high ionic conductivity.[18,19]

Alkali oxide GSEs are stable in ambient conditions and easily processable but have low ionic conductivities (10^{-7}–10^{-9} S cm^{-1} at 25 °C).[20] In contrast, sulfide GSEs have higher ionic conductivities (typically $\geq 10^{-4}$ S cm^{-1}) and lower processing temperatures than oxide GSEs.[21] However, sulfide-based GSEs are unstable in ambient conditions and in contact with lithium metal.[22] The mixture of oxide and sulfide GSEs leads to the formation of mixed oxy-sulfide (MOS) GSEs that combine the advantages from both parent glasses of easy processability and high ionic conductivities (10^{-3}–10^{-4} S cm^{-1} at 25 °C).[14,23] Furthermore, a new class of MOS-nitride (MOSN) GSEs can be created through the addition of nitrogen to these MOS GSE compositions. In this work, we have shown that adding nitrogen can improve the air stability of GSEs, stabilize the electrolyte in contact with lithium metal, and even improve the critical current density.[24,25] Also, MOSN GSEs have been found to display a combination of the positive properties of each respective parent glass.[24,25] For these reasons, MOSN GSEs have become as attractive as SSEs in ASSLBs.

Work completed by Bates and Dudney et al. demonstrated that incorporating nitrogen into oxide glasses enhances their ionic conductivity and significantly improves their electrochemical stability when in contact with lithium metal.[26] For instance, LiPON thin films have demonstrated over 10 000 cycles with 95% capacity retention, highlighting their robustness in long-term cycling.[27] Structurally, GSEs exhibit inherent flexibility and the ability to undergo shear deformation, which helps in accommodating volume changes during charge–discharge cycles, thereby enhancing the mechanical integrity of the battery.[28] In the work completed by Zhao et al., doping with oxygen and nitrogen was shown to stabilize the solid electrolyte interface and increase the critical current density, reaching up to 1.8 mA cm^{-2} at 100 °C.[25] This adaptability is crucial for preventing dendrite formation and ensuring stable interfaces between the electrolyte and electrodes. This study reports expands on the investigation of the structure and properties of these MOSN GSEs to better understand the electrochemical performance advantages of these new nitrogen-doped GSEs. A comparative table is provided in the ESI in Fig. S6† that shows how the properties of these GSEs compare to current electrolytes that do and do not use LiPON and are in roughly the same family of GSEs.

In the previous work on these MOSN GSEs, the short-range order (SRO) structures present in the mixed glass former (MGF), Si and P, GSE series $58.3Li_2S + 31.7SiS_2 + 10[(1 − x)Li_{0.67}PO_{2.83} + xLiPO_{2.53}N_{0.31}]$ $0 \leq x \leq 0.36$ (LiPSiSON) were investigated.[29] Due to the high Li_2S content (greater than 50%) in these GSEs, these materials are often referred to as invert glasses.[30,31] This work was the first report on MGF MOSN GSEs synthesized by the melt-quenching method. The compositional

dependence of the glass transition (T_g), crystallization temperatures (T_c), and working ranges (ΔT) was investigated, along with the validation of the presence of nitrogen in these GSEs. The findings confirmed that these MGF MOSN GSEs have improved properties and systematic structural changes when adding nitrogen. However, the ionic conductivity and the impact of LiPON incorporation on lithium ions' mobility were not studied previously.

The SRO structures of these MGF MOS GSEs have been thoroughly examined,[32–35] and now we further advance the study of these MGF MOSN GSEs by investigating the impact of the addition of LiPON on other physical properties of these GSEs, particularly the ionic conductivity and electrochemical stability. These MGF MOSN GSEs exhibit some of the highest reported ionic conductivities ($\sim 10^{-3}$ mS cm^{-1}) among bulk MQ GSEs. This new work, therefore, focuses on the ionic conductivity, activation energy (ΔE_{act}) and electrochemical stability of these GSEs. In particular, the Christensen–Martin–Anderson–Stuart (CMAS) model is used to calculate the binding energy (ΔE_B) and strain energy (ΔE_S) for these GSEs.[36] To use the CMAS model for these materials, it was necessary to measure all of the elastic moduli of these GSEs. All measured elastic moduli follow similar trends, exhibiting maxima or minima at $x = 0.12$. Overall, these GSEs exhibit high ionic conductivities with added LiPON, >1 mS cm^{-1} at 25 °C. However, these GSEs also exhibit a maximum in the ionic conductivity at $x = 0.12$. Surprisingly, this maximum is correlated with a minimum in the limiting high-frequency permittivity, which should have led to a maximum in the ΔE_{act}. Instead, the maximum in the conductivity is correlated with a minimum in the density, a maximum in the calculated free volume of the GSEs, and the fraction of doubly bonded nitrogen species, N_d, in these GSEs.

2. Experimental

2.1 Sample preparation

These GSEs were prepared following the methods described by Torres et al.[29] in an N_2 glovebox using as-received Li_2S (Alfa Aesar 99.99%) and in-house synthesized $Li_{0.67}PO_{2.83}$, $LiPO_{2.53}N_{0.314}$, and SiS_2. Glass samples were cast on a preheated mold set to 40 °C below the T_g, annealed for 3 hours, and then cooled at a rate of 1 °C min^{-1} to room temperature. Samples were dry-polished to ~1 μm, and gold contact electrodes were sputtered onto the samples using an Anatech Hummer VI Sputtering System inside the glovebox. Depending on the measurement, 2–3 mm thick, 14 mm diameter discs were prepared for low-frequency (0.01 Hz to 10 MHz) impedance measurements, while 1.5–2 mm thick, 6 mm diameter discs were used for high-frequency (1 MHz to 3 GHz) impedance measurements.

2.2 Physical properties

2.2.1 Density, molar volume, ionic volume, and free volume. Using Archimedes' principle, density measurements were made inside an Ar glovebox, <5 ppm H_2O and O_2, on melt-quenched GSE samples. Dried mineral oil with a density of 0.83

Table 1 List of equations used to calculate the mechanical moduli and Poisson ratio

Mechanical property	Equation
Longitudinal modulus (L)	$L = \rho v_L^2$ (1)
Shear modulus (G)	$G = \rho v_T^2$ (2)
Bulk modulus (K)	$K = L - \dfrac{4}{3}G$ (3)
Young's modulus (E)	$E = (1 + v)2G$ (4)
Poisson's ratio (v)	$v = \dfrac{L - 2G}{2(L - G)}$ (5)

$\pm\ 0.01$ g cm^{-3} was used as the immersion fluid. The molar volume (V_m) was calculated from the GSE's density and formula weight. The ionic molar volume (V_i) was calculated for each GSE using the Shannon ionic radii (r_k) for the different elements (k) present in the GSE.[37] The free volume (V_f) of the GSE is the calculated difference between V_m and V_i. The method and equations have been described in a previous publication.[14]

2.2.2 Sound velocity and mechanical moduli measurements. The longitudinal (v_L, m s^{-1}) and transverse (v_T, m s^{-1}) sound velocities were measured using an Ultratek EUT3160 pulser/receiver. The probe was equipped with a 15 MHz longitudinal and a 5 MHz transverse contact transducers. Vaseline and phenyl salicylate (Salol), respectively, were employed as the coupling agents for longitudinal and transverse measurements. The mechanical moduli of the GSEs were determined from the measured density and sound velocity measurements using equations given in Table 1. The thickness of the polished sample was measured across five different points on the GSE sample. The mechanical moduli and Poisson's ratio (v) of each GSE were then calculated from these four measured parameters, thickness (t), density (ρ), longitudinal velocity (v_L), and transverse velocity (v_T), using eqn (1)–(5), given in Table 1.

2.3 Dielectric spectroscopy

2.3.1 Impedance spectroscopy measurements. Ionic conductivity measurements of the GSEs were taken over a temperature range of -60 °C to 120 °C using isothermal low-frequency scans from 0.1 Hz to 7 MHz using an Alpha Analyzer and isothermal high-frequency scans from 1 MHz to 3 GHz using an Agilent E4991A RF Impedance/Material Analyzer on a Novocontrol Concept 80 dielectric spectrometer. Low- and high-frequency impedance spectroscopy samples were loaded into a custom air-tight sample holder inside an N$_2$ glovebox and an AG7 coin cell inside an Ar glovebox, respectively. Resistance (R) values were determined from the best fits of the complex impedance plot using a parallel R-constant phase element circuit. The ionic conductivity was calculated using eqn (6), where $\sigma(T)$ is the temperature-dependent ionic conductivity, t is the thickness of the GSE, A is the area of the sputtered Au electrodes, and $R(T)$ is the temperature-dependent resistance. The thicknesses of the samples were averaged from five different measurements.

$$\sigma(T) = \left(\frac{1}{R(T)}\right)\left(\frac{t}{A}\right) \quad (6)$$

2.3.2 Permittivity measurements. High-frequency dielectric permittivity (ε_∞) values were measured at 3 GHz and -140 °C (which, due to liquid N$_2$ cooling, -140 °C (130 K) was the coldest temperature that could be reached) using the Novocontrol Concept 80 dielectric spectrometer and Agilent E4991A RF Impedance/Material Analyzer. The ε_∞ values were taken from the high-frequency impedance spectroscopy measurement of the permittivity in the flattest region of the permittivity data around 3 GHz. The AG7 coin cell and custom sample cell holder were calibrated with a Teflon standard, $\varepsilon_\infty = 2.1$, to determine the stray capacitance and to ensure accurate permittivity measurements.

2.4 Electrochemical characterization

Time dependent EIS and galvanostatic cycling were conducted using a Biologic VMP-300 potentiostat in a dual plunger style cell. Approximately, 1 gram of the GSEs were spex milled for 5 min inside of an N$_2$ glovebox with <0.1 ppm of H$_2$O and O$_2$. 100 mg of glass powder was removed from the spex mill and pressed into a 10 mm diameter die for 2 minutes at 400 MPa of pressure. Cells were fabricated inside an Ar glovebox with <0.1 ppm of H$_2$O and O$_2$ using Li|GSE|Li inside of a CR2032 type coin cells with electrode areas less than 1 cm^2. EIS scans were collected every 10 min for approximately 28 h from 7 MHz to 0.1 Hz with a 25 mV excitation voltage. Critical current density measurements were determined through step increasing the current at the end of a cycle.

3. Results and discussion

3.1 Brief review of the structure of LiPSiSON GSEs

We have previously reported on the SRO structure of these $58.3\text{Li}_2\text{S} + 31.7\text{SiS}_2 + 10[(1 - x)\text{Li}_{0.67}\text{PO}_{2.83} + x\text{LiPO}_{2.53}\text{N}_{0.314}]$, where $0 \leq x \leq 0.36$ MGF MOSN GSEs.[29] When LiPON is combined with a MOS glass, the resulting MGF MOSN GSE contains unique structures that impact the properties of these GSEs. Therefore, these LiPSiSON GSEs contain a mixture of SRO structures, including silicon bonded to sulfur and oxygen and phosphorus bonded to sulfur, oxygen, and nitrogen, with no evidence found of silicon being bonded to nitrogen. With the creation of covalent phosphorous–nitrogen bonds from the addition of LiPON to maintain charge balance, there is a corresponding increase in non-bridging oxygen (NBO) sites on phosphorus and silicon. These NBO sites are undesirable as they create higher activation energy sites for lithium ions, decreasing the ionic conductivity. Fourier Transformation Infrared (FTIR), Raman, ^{29}Si NMR, and ^{31}P NMR, combined with charge balancing requirements, were used to determine the SRO structures of these LiPSiSON GSEs and were interrogated to explain the changes observed in the T_c and T_g of these GSEs. (Specific details for the experimental parameters, instrument models, and testing conditions that were used to collect the spectroscopic data can be found in Torres *et al.*).[29]

The glassy nature of these samples was verified by combining powder X-ray diffraction with DSC to show that these MGF MOSN GSEs were X-ray amorphous and exhibited a T_g. The
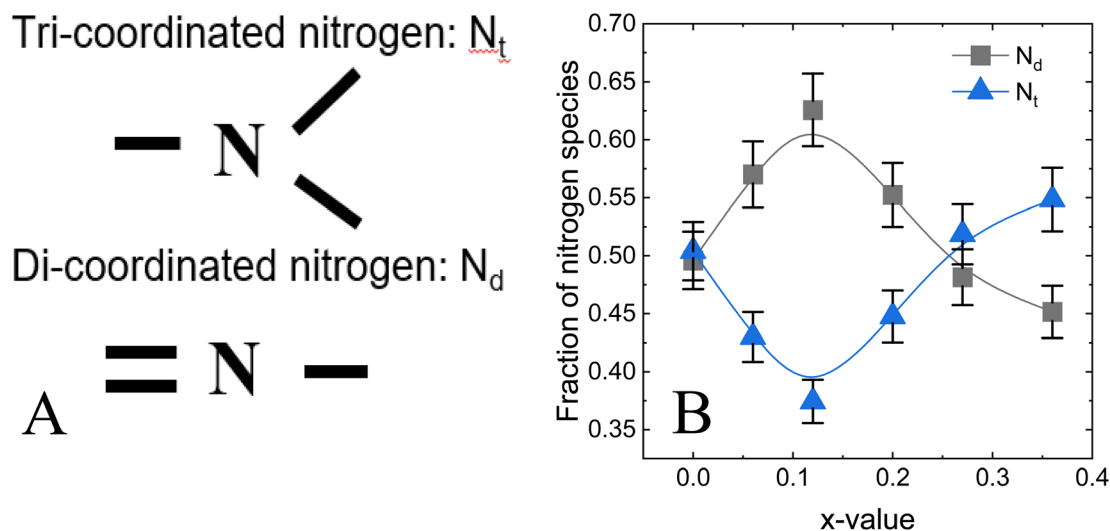
Fig. 1 (A) The depiction of the bonding arrangement for the nitrogen species and (B) the fraction of nitrogen species determined from the N 1s XPS spectra for $58.3Li_2S + 31.7SiS_2 + 10[(1-x)Li_{0.67}PO_{2.83} + xLiPO_{2.53}N_{0.314}]$ series for $0 \leq x \leq 0.36$.

DSC thermal scans also showed that adding LiPON increased the T_c to a maximum of 475 °C for the $x = 0.12$ sample. The amount and types of nitrogen in these GSEs were analyzed using a combination of XPS and sulfur and nitrogen combustion analysis, revealing the presence of both tri-coordinated (N_t) and di-coordinated (N_d) species in the glass structure with a depiction of these bonds displayed in Fig. 1A. With increasing LiPON incorporation, N_d exhibits a maximum. In contrast, N_t exhibits a minimum at $x = 0.12$ and can be observed in the graph in Fig. 1B. With further increasing LiPON content, the N_t increases, and N_d decreases. The presence of nitrogen was further substantiated using other spectroscopic analyses, including NMR, FTIR, Raman, and XPS spectroscopies. Systematic changes in key structural units such as the SiS_4^{4-}, $Si_2S_6^{6-}$, $P_2S_7^{4-}$, $P_2S_6^{4-}$, and MOS units bonded to phosphorous and silicon provide evidence of structural rearrangements corresponding to nitrogen incorporation. Third, as determined by combining charge balance requirements with the spectroscopic analysis of these GSEs, the SRO species exhibited systematic and distinct changes, with a general increase in phosphorous non-bridging sulfur (NBS) SRO units and a decrease in silicon non-bridging oxygen (NBO) SRO units. These changes indicate the energetic stability of the preferential bonding of phosphorus with sulfur and silicon with oxygen.[14,25,38]

3.2 Physical properties of LiPSiSON GSEs

The composition dependent density $\rho(x)$ of these glasses, shown in Fig. 2A, reveals a density of 1.96 g cm^{-3} in the base glass ($x = 0.00$). With the incorporation of LiPON, it decreases to a minimum value of 1.94 g cm^{-3} in the $x = 0.12$ GSE. Further additions of LiPON were found to increase the glass density, reaching 2.00 g cm^{-3} at $x = 0.36$. The molar volume was found to increase from 32.76 cm^3 mol^{-1} ($x = 0.0$) to a maximum value of 33.03 cm^3 mol^{-1} at $x = 0.12$, and then, with increasing x, the molar volume decreases to 31.94 cm^3 mol^{-1} at $x = 0.36$. The

calculated ionic volume, also shown in Fig. 2B, increases linearly from 21.63 cm^3 mol^{-1} at $x = 0.0$ to 21.71 cm^3 mol^{-1} at $x = 0.36$. The free volume was calculated from the difference between the molar and ionic volumes and is shown in Fig. 2C. The free volume at $x = 0.0$ is 11.13 cm^3 mol^{-1}, increasing to a maximum value of 11.37 cm^3 mol^{-1} at $x = 0.12$, followed by a decrease to 10.23 cm^3 mol^{-1} at the highest LiPON concentration. These variations in density, molar volume, and free volume suggest underlying structural changes in the glass network. This can be better understood by examining the role of non-bridging anion, NBO and NBS species, and nitrogen species and their influence on glass connectivity.

Upon further investigation, the trends observed in the density, molar volume, and free volume are consistent with the composition dependence of the concentrations of NBSs, NBOs, and the N_t species. The more highly coordinated N_t SRO unit crosslinks the glass structure more effectively than the doubly coordinated N_d SRO units. As a result, the glass network expands to create a more uncompressed glass network with additional sites for Li$^+$ ions to occupy. Similar trends in the density and molar volumes have been observed for related compositions.[14,18,39–41] Furthermore, the subsequent increase in density is due to the increase in tri-coordinated nitrogen species from the addition of LiPON. The presence of N_t species promotes the formation of more non-bridging oxygen sites, which surround the nitrogen and, in turn, contract the network and lead to the immobilization of lithium ions. A full table of the densities, molar volume, ionic volume, and free volume can be found in Table S1.†

These inverted GSEs differ from their covalent network counterparts due to the predominance of ionic bonding. As a result, these GSEs exhibit a fragmented network composed mainly of isolated, non-networked tetrahedra. Consequently, the mechanical properties are likely governed more by the ionic interactions between the individual ionic SRO species.[42]
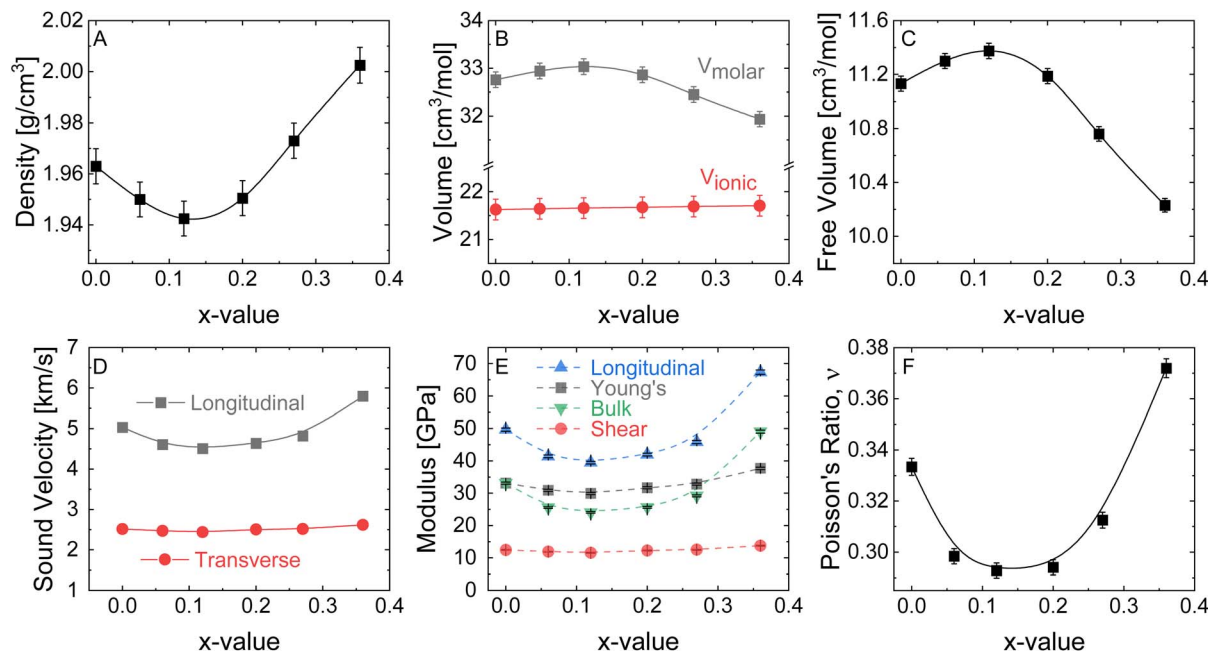
Fig. 2 (A) Compositional dependence on density measurements measured in g cm^{-3}, (B) ionic and molar volume measured in cm^3 mol^{-1}, (C) free volume measured in cm^3 mol^{-1}, (D) longitudinal and transverse sound velocity measured in km s^{-1}, (E) mechanical moduli (the graph lists the Longitudinal, Young's, Bulk, and Shear Moduli) measured in GPa, and (F) Poisson's ratio, which is unitless, of glasses in the series 58.3Li$_2$S + 31.7SiS$_2$ + 10[(1 − x)Li$_{0.67}$PO$_{2.83}$ + xLiPO$_{2.53}$N$_{0.314}$] $0 \leq x \leq 0.36$.

The composition dependent longitudinal and transverse velocities, mechanical moduli, and Poisson's ratio of these GSEs were determined using eqn (1)–(5) and are shown in Fig. 2D–F. The longitudinal and transverse velocities, along with the mechanical moduli, as well as Poisson's ratio, exhibit trends similar to the density measurements, decreasing to a minimum at $x = 0.12$ before increasing with further LiPON incorporation. The values of the sound velocities and mechanical moduli are found to be consistent with similar compositions reported in the literature.[43,44] Upon the initial incorporation of LiPON, there is an overall increase in the N$_d$ species, corresponding to a decrease in sound velocities and mechanical moduli, with a minimum at $x = 0.12$ displayed in Fig. 2D–F.[29] The GSE with a higher concentration of N$_d$ species at $x = 0.12$ is more easily compressed due to its greater free volume and lower network density (Fig. 2B). However, as LiPON content increases, the proportion of N$_t$ species also rises, leading to a denser glass network with reduced free volume. This structural change results in higher velocities, moduli, and Poisson's ratio, making the material more resistant to compression. Similar values for the sound velocities, mechanical moduli, and Poisson's ratios have been observed in the literature.[23,44] A full table of the sound velocity measurements and mechanical moduli/properties is recorded in Table S2.†

3.3 Impedance spectroscopy of the LiPSiSON GSEs

3.3.1 Low-frequency and high-frequency impedance spectroscopy. The temperature-dependent ionic conductivities of these GSEs were initially measured using low-frequency, 0.01 Hz to 10 MHz, EIS for all these LiPSiSON GSEs. The

temperature-dependent bulk electrolyte resistances were extracted from the Nyquist plots in the customary manner. Fig. 3A shows the low-frequency impedance data (black points) for typical behavior in the low-temperature regime.

The average electrical relaxation time of the glass (τ) is given in eqn (7), where R is the equivalent circuit DC resistance, C is the equivalent circuit capacitance, ε_0 is the permittivity of free space, ε_∞ is the high-frequency relative permittivity, and σ_{dc} is the DC ionic conductivity.

$$\tau \approx RC = \left(\frac{\varepsilon_0 \varepsilon_\infty}{\sigma_{dc}}\right) \quad (7)$$

In the low temperature low conductivity regime, τ is sufficiently long enough that the frequency range of the low-frequency analyzer can span the range where $1/f_{low} \gg \tau \gg 1/f_{high}$, where f_{low} and f_{high} are the low- and high-frequency limits, given above, of the impedance analyzer. In this case, the resulting complex impedance plot consists of a full or nearly full semi-circle arc in the complex plane. Therefore, ε_∞ and σ_{dc} can be accurately determined from non-linear least square fits of the impedance data, demonstrating that the impedance plot in Fig. 3A provides sufficient data to precisely determine the temperature-dependent ionic conductivity.

However, at higher temperatures, τ reduces exponentially with the exponential increase in ionic conductivity. As a result, even at the high-frequency limit of the spectrometer, 10 MHz, $\tau \ll 1/f_{high}$, and the measured complex impedance data no longer exhibits a semi-circle arc. Instead, now in this temperature range, the ionic motion has become so fast and τ so short that only the space charge polarization capacitance is observed, as shown in Fig. 3B as the polarization spike (Warburg).
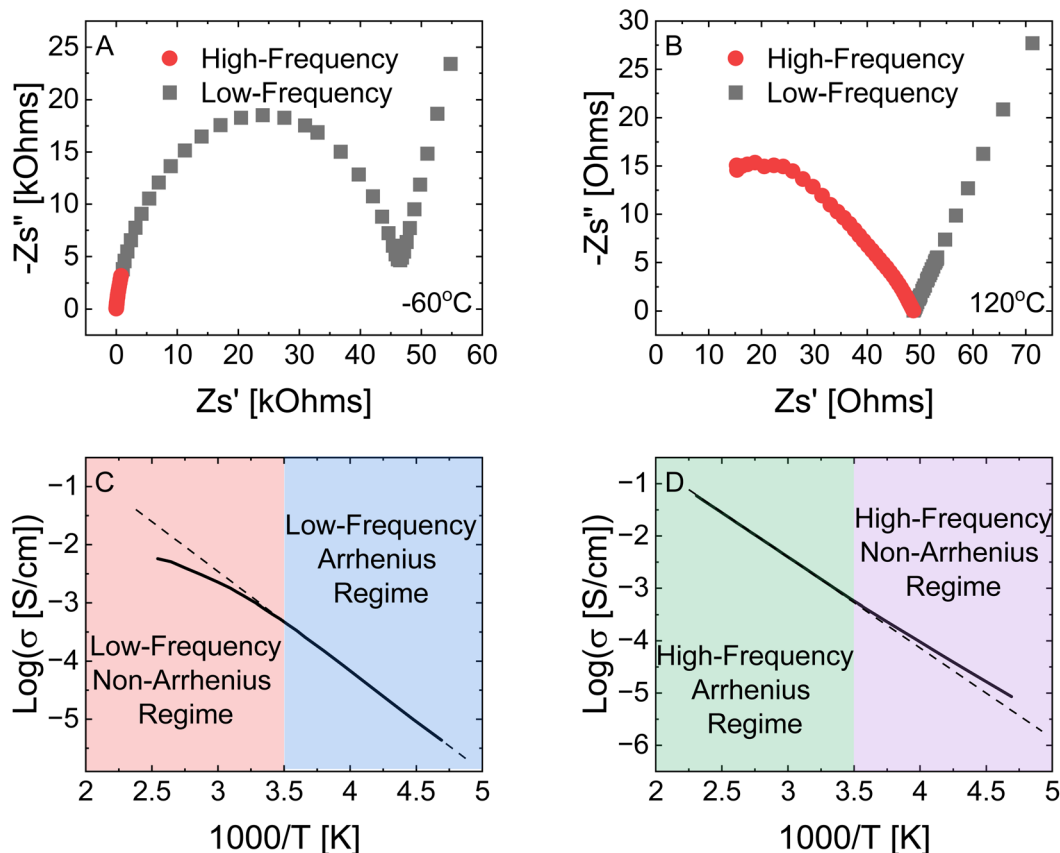
Fig. 3 High-frequency and low-frequency electrochemical impedance spectroscopy Nyquist plots of the $x = 0$ GSE for temperatures (A) -60 °C with the y-axis measured in k Ohms and x-axis measured in Ohms and (B) 120 °C with the y- and x-axis measured in Ohms. (C) Low-frequency Arrhenius plot of the $x = 0$ GSE for temperatures between -60 and 120 °C, where the data deviates from linear behavior at higher temperatures above 10 °C. The dashed line guides the eye for the expected Arrhenius behavior. (D) High-frequency Arrhenius plot of the $x = 0$ GSE for temperatures between -60 °C and 160 °C. The data deviated from linear behavior at lower temperatures below 10 °C. Both (C) and (D) were measured with the y-axis in a logarithmic scale of S cm^{-1} and the x-axis in a inverse scale of temperature of K.

Such polarization spikes can give inaccurate and elevated equivalent circuit impedance values. As an example of this, Fig. 3C shows the Arrhenius temperature dependence of the conductivity determined for the $x = 0$ GSE using only the low-frequency impedance analyzer. This plot exhibits deviations from linearity at temperatures above 10 °C. In this temperature range, the ionic conductivity is sufficiently high so that only polarization can be observed, such as that seen in Fig. 4B. The low-frequency non-Arrhenius high temperature and Arrhenius low-temperature regimes are shaded red and blue, respectively. Although low-frequency electrochemical impedance spectroscopy measurements are commonplace, the advent of many SSEs, whose conductivities exceed 1 mS cm^{-1} at room temperature, has made accurate determinations of their ionic conductivities more challenging. Therefore, high-frequency measurements, $f_{high} > 1$ GHz, were utilized in this work to overcome the low-frequency polarization behavior described above to provide access to the rest of the semicircle on the Nyquist plots so that more accurate determinations of the ionic conductivities and activation energies could be made.

As shown in Fig. 3A and B, while the low-frequency analyzer can accurately determine the complex plane plot at low temperatures, here, even the low-frequency limit of the high-frequency analyzer, 1 MHz, is too high to collect impedance data over the whole arc. The opposite is true for the high-temperature range data. The high-frequency limit of the low-frequency analyzer is too low to show the whole arc, whereas the high-frequency analyzer can resolve the whole impedance arc. Fig. 3D shows the Arrhenius plot of the DC conductivity for the $x = 0$ GSE determined using the high-frequency analyzer. It exhibits deviation from linearity at temperatures below 10 °C, where the frequencies are now too high, and the conductivities are too low to accurately resolve the full complex impedance arc.

For these reasons, both low- and high-frequency impedance measurements were collected for these GSEs to accurately determine the full wide temperature range of the DC conductivities of these highly conducting LiPSiSON GSEs.

3.3.2 Combined Arrhenius plot of low-frequency and high-frequency data. An Arrhenius plot that combines the low- and high-temperature data is shown in Fig. 4A. The composition-dependence (x) of the room temperature ionic conductivities, $\sigma_{ionic}(x)$, taken from Fig. 4A are shown in Fig. 4B, along with the activation energies (ΔE_{act}), best fit to the Arrhenius equation. With the addition of LiPON, the ionic conductivity increases
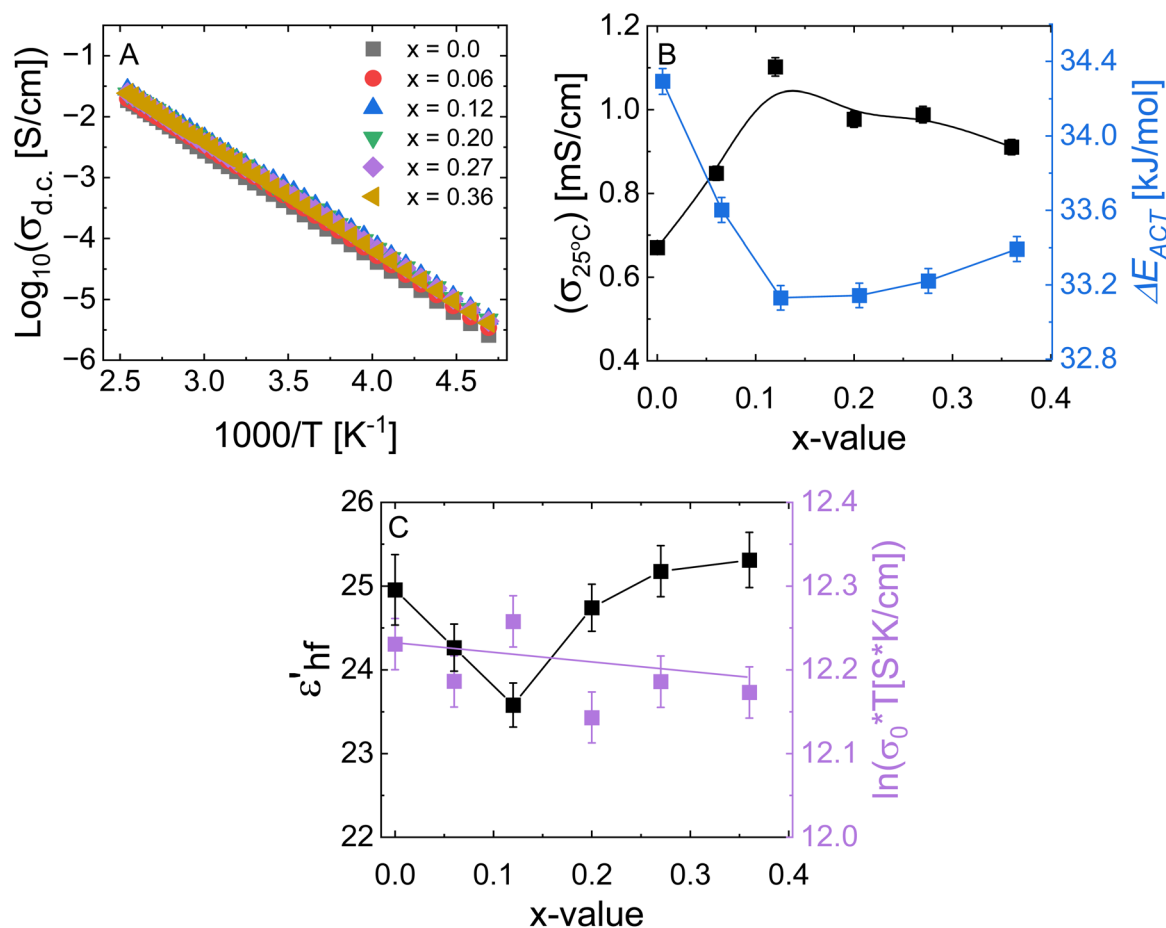
Fig. 4 (A) Arrhenius plot of the temperature-dependent ionic conductivity for the GSEs in the series $58.3Li_2S + 31.7SiS_2 + 10[(1-x)\,Li_{0.67}PO_{2.83} + xLiPO_{2.53}N_{0.314}]$ $0 \leq x \leq 0.36$ from −60 to 130 °C. The ionic conductivity is measured in S cm^{-1} and the graph is displayed in a logarithmic scale. Graph of the (B) ionic conductivity at 25 °C (σ_{ionic}, black) measured in mS cm^{-1}, activation energies (ΔE_{act}, blue) measured in kJ mol^{-1}, (C) high-frequency relative permittivity (ε'_{hf}, black) which is unitless, and the pre-exponential factor multiplied by temperature ($\sigma_0 \times T$, purple) which is measured in (S × K cm^{-1}).

from 0.67 mS cm^{-1} at $x = 0$ to a maximum of 1.1 mS cm^{-1} at $x = 0.12$ before decreasing to 0.91 mS cm^{-1} at $x = 0.36$.

ΔE_{act} follows an inverse trend to the room temperature ionic conductivity, where the activation energy at $x = 0$ is 34.3 kJ mol^{-1}.[36,42,45–47] The activation energy then decreases to a minimum of 33.1 kJ mol^{-1} at $x = 0.12$ and increases to 33.4 kJ mol^{-1} at $x = 0.36$. The presence of N_d species was found to increase the free volume in the glass network, giving rise to higher ionic conductivity and lower activation energy for the $x = 0.12$ GSE. Like the physical properties discussed earlier, the increase in ionic conductivity is also found to correlate with the increase in N_d species. However, as LiPON incorporation increases, ΔE_{act} rises while the ionic conductivity decreases. This change is correlated to the maximum ratio of N_d species, a subsequent increase in N_t species, and the formation of more NBO sites within these glasses.[29]

As will be shown below, the limiting high frequency permittivity, ε_∞, is an important factor also controlling ΔE_{act}. As described above, it cannot be measured at room temperature as the lithium ions motions are active and not frozen out as required in determining ε_∞ was not able to be collected for

these materials at room temperature as the lithium ions are too fast. Therefore, cooling the samples to −140 °C and leveraging high frequency measurements at $f_{high} = 3$ GHz, a broader temperature and frequency space where $\tau \gg \frac{1}{\omega} = \frac{1}{2\pi f}$ was accessed. At −140 °C, Fig. 5A shows that the conductivity has reduced to $\sim 1 \times 10^{-10}$ S cm^{-1}. At this temperature, τ is 100 seconds, equivalent to ~ 1 mHz. Hence, at 1 GHz and −140 °C, the electric field change is 10^{12} times faster than the average electrical relaxation time. For this reason, the electrical response of the GSE will be dominated by the electronic polarizability of the stationary ions in the GSE and thereby give rise to accurate measurements of the ε_∞. Hence, the conditions of 1 GHz and −140 °C were used to determine the ε_∞ values. The composition dependence of the high-frequency relative permittivity ($\varepsilon'_{hf} \approx \hat{\varepsilon}_\infty$) and the pre-exponential factor (σ_0) of these GSE are given in Fig. 4C.

Accurately determining the permittivity values for these materials was a rather intensive process as these GSEs have such high conductivities that low temperatures, −140 °C, were required to get accurate and reliable values by freezing out the
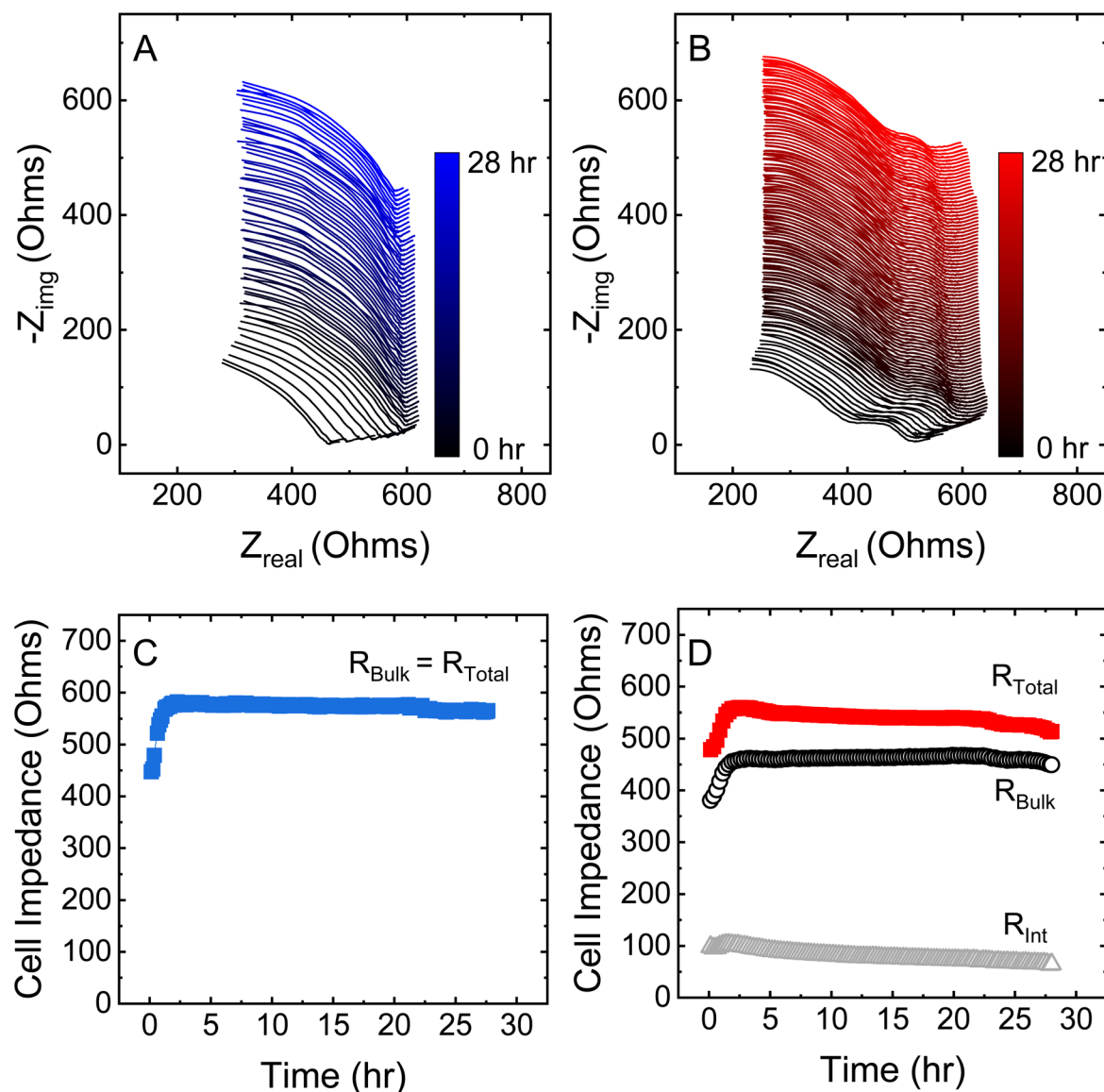
Fig. 5 Nyquist plot for (A) the Li|LiPSiSO|Li ($x = 0$ GSE) and (B) Li|LiPSiSON|Li ($x = 0.12$ GSE) symmetric cell scanned every 30 min for 12 h. (C) and (D) show the equivalent circuit fitted resistance values for the Nyquist plots shown in (A) and (B), showing that the $x = 0$ GSE does not have any interface form for the material whereas the $x = 0.12$ GSE forms an interface at around 100 Ohms.

mobile cation contribution to the dielectric polarizability. The method and work involved to determine $\varepsilon'_{hf}\hat{\varepsilon}'_{\infty}$ is discussed further in the ESI and is shown in Fig. S1.† ε'_{∞} decreases from 25 at $x = 0.00$ to a minimum at $x = 012$ of 23.58 and increases to 25.31 at $x = 0.36$, following a similar trend to the ΔE_{act}. This trend is opposite of what is expected: a lower permittivity would suggest smaller shielding of the collective coulomb forces acting on the cation and this would be expected to lead to a higher activation energy. However, comparing Fig. 4C to 1A, above, the minimum in ε_{∞} corresponds to a maximum in N_d and a minimum in N_t species in these glasses. It is consistent that the doubly bonded nitrogen may be a less polarizable, higher electron binding energy species, and cause the lower ε_{∞} values. The opposite correlation to the compositional trends in the ΔE_{act} suggests other factors controlling its composition dependence. We will investigate that below.

The σ_0 values remain essentially constant at $\ln(\sigma_0) \sim 12$ K Ω^{-1} cm^{-1}, similar to values for the pre-exponential factor observed in comparable GSEs.[14,23] A table of the room temperature σ_{ionic}, ΔE_{act}, ε_{∞}, and σ_0 values can be found in Table S3.†

3.4 Electrochemical stability of LiPSiSON GSEs with Li-metal electrodes

To identify the effects of nitrogen on the electrochemical stability of these MOSN GSE, the $x = 0$ and $x = 0.12$ GSEs in this series $58.3Li_2S + 31.7SiS_2 + 10[(1 - x)Li_{0.67}PO_{2.83} + xLiPO_{2.53}$-$N_{0.314}]$, $0 \leq x \leq 0.36$ were tested in lithium symmetric cells for ~30 hours. The time-dependent Nyquist plots are shown in Fig. 5A and B for $x = 0$ and $x = 0.12$, respectively, alongside the extracted resistance values from equivalent circuit fits in Fig. 5C and D.

For both samples, the cell resistance increased during the first few hours before stabilizing for the remainder of the experiment. Without nitrogen ($x = 0$), the Nyquist plot shows a single semicircle attributed to the bulk resistance ($\sim$580 Ω), Fig. 5C. In contrast, the nitrogen-containing sample ($x = 0.12$), shown in Fig. 5D, exhibits two arcs: the high-frequency arc representing the bulk resistance ($\sim$450 Ω) and the second arc representing the interfacial resistance ($\sim$100 Ω). The $x = 0$ GSE, which lacks LiPON doping and contains no nitrogen, shows no interface formation, presenting only bulk resistance. Although both the $x = 0$ and $x = 0.12$ cells exhibit nearly identical bulk resistance values, the nitrogen-containing $x = 0.12$ GSE possesses a distinct interfacial feature (with a unique time constant) not observed in the baseline $x = 0.00$ composition. This interfacial contribution has been tentatively attributed to the formation of Li_3N-based species at the lithium metal–solid electrolyte interface. The presence of this stable interface facilitates charge transfer and effectively lowers the overall resistance, making the $x = 0.12$ MOS GSE a more promising electrolyte candidate for solid-state batteries. This behavior aligns well with literature reports on the beneficial interfacial properties imparted by LiPON doping.[26,48,49]

In addition to testing the electrochemical stability of these GSEs with lithium metal, galvanostatic stripping/plating experiments were conducted (Fig. 6A and B). For these measurements, Li symmetric cells were cycled at 0.1, 0.2, and 0.4 mA cm^{-2}, with 10 charge/discharge cycles at each of the first two current densities, followed by 35 charge/discharge cycles at the final current density. While both cells successfully stripped and plated lithium at low current densities, extended cycling at 0.2 mA cm^{-2} caused the $x = 0$ GSE to short after approximately 30 hours. This short circuit is attributed to the absence of a stable interface between the GSE and the lithium metal.[10,50–52] In contrast, galvanostatic cycling of the nitrogen-containing glass (Fig. 6B) showed stable performance up to $\sim$110 hours.

Beyond this point, the cell began to show signs of degradation, indicative of increased cell resistance.

3.5 CMAS model – activation energy in LiPSiSON GSEs

We now return to the questions generated concerning the composition dependence of ΔE_{act} in these MGF MOSN GSEs and better understand the apparent anti-correlation of ΔE_{act} with ε_∞ and its apparent correlation to the concentration of N_d SRO units in these GSEs. Anderson and Stuart (AS) were among the first to develop a model of the ΔE_{act} of GSEs in terms of the structure and other physical properties of the glass.[53] Further explanation and background on the development of the AS model can be found in the ESI.† ΔE_{act} can be written as the sum of ΔE_S and ΔE_B, given in eqn (8).

$$\Delta E_{act} = \Delta E_S + \Delta E_B \tag{8}$$

As a refinement to the AS original model, McElfresh and Howitt argued that the strain energy determined by AS failed to properly account for an atom's diffusion through a solid.[54] Furthermore, the strain energy did not properly account for the jump distance of the mobile cation, nor did it properly account for the size relationship between the mobile cation and the effective size of the interstitial site between cation sites. McElfresh and Howitt's expression for strain energy is given in eqn (9) and consists of four parameters: the shear modulus (G), the lithium-ion jumping distance (λ_{Li^+}), the radius of a lithium-ion (r_{Li^+}), and the doorway radius (r_D).

$$\Delta E_S = N_A \pi G \left(\frac{\lambda_{Li^+}}{2}\right)(r_{Li^+} - r_D)^2 \tag{9}$$

Christensen and Martin further refined and improved the original AS model by providing a more accurate estimate of the ΔE_B term by accounting for the fact that the binding energy should vanish at zero jump distance, where the cation has not moved from its equilibrium position.[29] Eqn (10) gives the CMAS model for the coulombic binding energy, ΔE_B. The binding energy is the electrostatic binding energy needed to create mobile charge carriers in the GSE.

$$\frac{\Delta E_B}{M_C} = \frac{Z_{Li^+} Z_{X^-} e^2}{4\pi\varepsilon_0\varepsilon_\infty}\left(\frac{1}{r_{Li^+} + r_{X^-}} - \frac{1}{r_{Li^+} + r_{X^-} + (\lambda_{Li^+}/2)}\right) \tag{10}$$

In this expression, M_C is the effective Madelung constant, Z_{Li^+}, and Z_{X^-} are the charges on the cation and the anion X^- (O^- or S^-), e is the charge of an electron, ε_∞ is the high-frequency relative permittivity, r_{Li^+} is the radius of the cation, and r_{X^-} is the radius of the X^- anion. Because M_C cannot be calculated explicitly for disordered materials, it was estimated through eqn (11) using the experimental activation energy, $\Delta E_{act,}$ and the values measured from the binding and strain energy.

$$M_C = \frac{\Delta E_{Act} - \Delta E_S}{(\Delta E_B / M_C)} \tag{11}$$
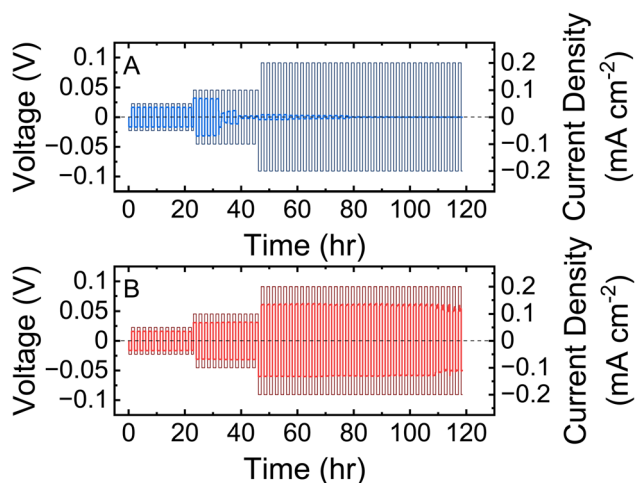

Fig. 6 Step-increased current density testing for (A) the Li|LiPSiSO|Li ($x = 0$ GSE) and (B) Li|LiPSiSON|Li ($x = 0.12$ GSE) symmetric cell. The $x = 0$ GSE shorted after $\sim$30 hours while the $x = 0.12$ GSE did not display any degradation until $\sim$110 hours.

Fig. 7A shows the composition dependence of ΔE_S determined using eqn (9) and the physical properties described above. The

ΔE_S is 1.13 kJ mol^{-1} at $x = 0$ and decreases to a minimum of 1.09 kJ mol^{-1} at $x = 0.12$, which is essentially unchanged. However, this minor decrease is consistent with the minimums observed in all of the modulii of these GSEs and is also directly correlated to the increase in N$_t$ species. These trends are all consistent. The "triclusters" N$_t$ would be expected to cross-link the glass structure and thereby increase the mechanical modulii.

However, the strain energy is minimal, only comprising about 3% of the total measured conductivity activation energy, and therefore does not contribute significantly to the composition dependence of the conductivity activation energy. For this reason, the binding energy is the dominant term for the activation energy in these materials. Such behavior has been seen in many other alkali ion-conducting GSEs.[55–57]

Since as described above the M_C values cannot be calculated *a priori*, the ratio of the binding energy to the Madelung constant, $\Delta E_B/M_c$ was calculated using eqn (10) and is shown in Fig. 7B. The $\Delta E_B/M_c$ is 10.28 kJ mol^{-1} at $x = 0$ and increases to a maxim value of 10.83 kJ mol^{-1} at $x = 0.12$. The increase in the $\Delta E_B/M_c$ is consistent with the observed minimum in the ε_∞ and follows the maximum in the N$_d$ species for these GSEs. The $\Delta E_B/M_c$ decreases to a value of 9.92 kJ mol^{-1} at $x = 0.36$.

The calculated Madelung constant values, M_C, for these GSEs, were determined from eqn (11) and are given in Fig. 7C. The M_C is 3.22 at $x = 0$ and decreases to a minimum of 2.95 at $x = 0.12$. As more LiPON is added to the composition, the M_C increases to 3.23 at $x = 0.36$. These values for the Madelung constant are consistent with other SSEs and similar materials reported in the literature.[18,58]

LiPON is a unique material due to the presence of N$_d$ and N$_t$ species inside the glass network. From the addition of LiPON, these MGF MOSN GSEs retain these key SRO units. In specific, the nitrogen species are the main reason for the changes exhibited in the properties of these materials. In fact, Fig. 8 shows a strong correlation between the $\Delta E_B/M_c$ and the fraction of N$_d$ species. The increase in N$_d$ nitrogen corresponds to higher binding energy and a greater number of mobile lithium ions in the GSEs, making N$_d$ species a key factor in maximizing binding energy. After a LiPON content of $x = 0.12$, the binding energy declined, and in turn, the N$_d$ species decreased, and the N$_t$ species increased. This decrease in N$_d$ species, therefore, leads to the reduction in the binding energy, by limiting the concentration of mobile lithium ions in the materials. This correlation between the $\Delta E_B/M_c$ and the fraction of N$_d$ is shown in Fig. 8.
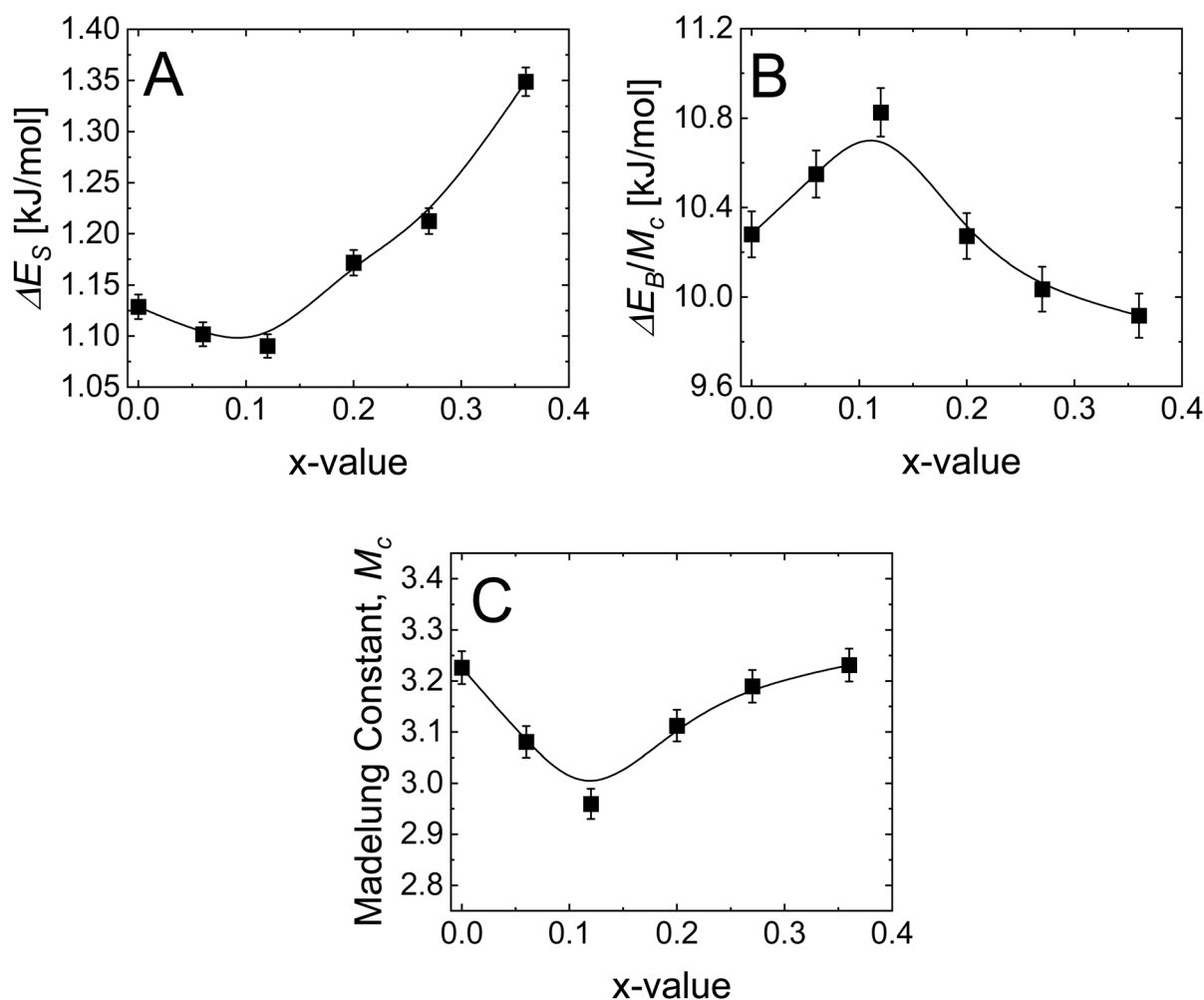

Fig. 7 Composition dependent (A) strain and (B) binding energy which are measured in kJ mol^{-1} and (C) Madelung constant which is unitless.
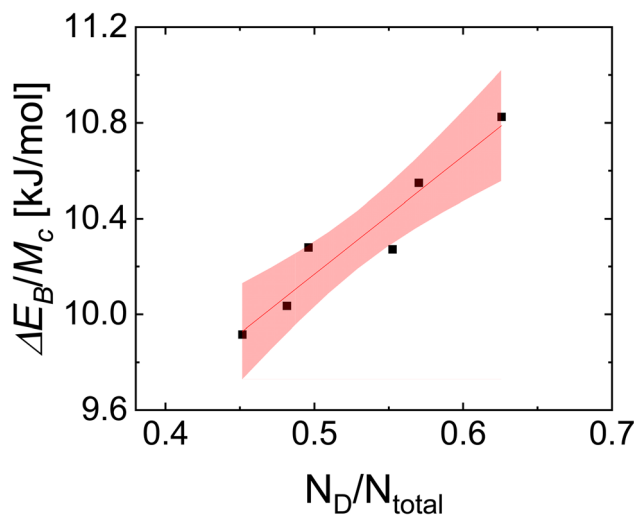
Fig. 8 Plot of the $\Delta E_B/M_c$ values, which are measured in kJ mol^{-1}, versus the fraction of N$_d$ species for the series 58.3Li$_2$S + 31.7SiS$_2$ + 10 [(1 − x)Li$_{0.67}$PO$_{2.83}$ + xLiPO$_{2.53}$N$_{0.314}$] with $0 \leq x \leq 0.36$. $\Delta E_B/M_c$ is correlated to N_d/N_{total} within a 95% confidence interval.

4. Conclusions

This report describes the investigation of the physical and electrochemical properties of a new class of materials: MOSN GSEs. The composition of the series is 58.3Li$_2$S + 31.7SiS$_2$ + 10 [(1 − x)Li$_{0.67}$PO$_{2.83}$ + xLiPO$_{2.53}$N$_{0.314}$] $0 \leq x \leq 0.36$. A previous study investigated the SRO structure of these GSEs, and this work aimed to further the analysis of these materials. The density displayed a minimum at $x = 0.12$, leading to a maximum in the free volume for the same composition. A minimum was also observed for the sound velocity measurements, various mechanical moduli, and Poisson ratio. Interestingly, the ionic conductivity measurements required high- and low-frequency measurements accurately measure the temperature dependence of the ionic conductivity of these GSEs. The addition of LiPON improved the electrochemical performance of these GSEs and led to stable cycling behavior along with a stable interfacial formation. The ionic conductivity displayed a maximum at $x = 0.12$ of 1.1 mS cm^{-1}, and the activation energy displayed a corresponding minimum for the same x-value. The CMAS model was used to show that the activation energy in these GSE is dominated by the binding energy. It has been found that adding LiPON into these MOS GSE systems leads to an overall positive impact on the material properties, especially density, free volume, ionic conductivity, and activation energy and this makes these MGF MOSN GSEs promising candidates for use in all-solid-state battery technology.

Data availability

The data supporting this article have been included as part of the ESI.†

Conflicts of interest

There are no conflicts to declare.

Acknowledgements

References

1 H. Wan, J. Xu and C. Wang, *Nat. Rev. Chem.*, 2024, **8**, 30–44.
2 M. Schiemann, J. Bergthorson, P. Fischer, V. Scherer, D. Taroata and G. Schmid, *Appl. Energy*, 2016, **162**, 948–965.
3 M. Ghiji, S. Edmonds and K. Moinuddin, *Appl. Sci.*, 2021, 11.
4 F. Larsson, P. Andersson, P. Blomqvist and B.-E. Mellander, *Sci. Rep.*, 2017, **7**, 10018.
5 N. Chawla, N. Bharti and S. Singh, *Batteries*, 2019, **5**, 19.
6 Y. Q. Chen, Y. Q. Kang, Y. Zhao, L. Wang, J. L. Liu, Y. X. Li, Z. Liang, X. M. He, X. Li, N. Tavajohi and B. H. Li, *J. Energy Chem.*, 2021, **59**, 83–99.
7 M. Armand and J.-M. Tarascon, *Nature*, 2008, **451**, 652–657.
8 Q. Zhao, S. Stalin, C.-Z. Zhao and L. A. Archer, *Nat. Rev. Mater.*, 2020, **5**, 229–252.
9 O. Sheng, C. Jin, X. Ding, T. Liu, Y. Wan, Y. Liu, J. Nai, Y. Wang, C. Liu and X. Tao, *Adv. Funct. Mater.*, 2021, **31**, 2100891.
10 J. Lau, R. H. DeBlock, D. M. Butts, D. S. Ashby, C. S. Choi and B. S. Dunn, *Adv. Energy Mater.*, 2018, **8**, 1800933.
11 T. Polczyk, W. Zajac, M. Ziabka and K. Swierczek, *J. Mater. Sci.*, 2021, **56**, 2435–2450.
12 J. Wheaton, S. Kmiec, D. Schuler, C. Sorensen and S. W. Martin, *ACS Appl. Energy Mater.*, 2021, **4**, 10835–10842.
13 R. Zhao, G. Hu, S. Kmiec, R. Gebhardt, A. Whale, J. Wheaton and S. W. Martin, *ACS Appl. Mater. Interfaces*, 2021, **13**, 26841–26852.
14 V. Torres III, P. Philipp, S. Kmiec and S. W. Martin, *Chem. Mater.*, 2024, **36**, 5521–5533.
15 X. Chi, Y. Zhang, F. Hao, S. Kmiec, H. Dong, R. Xu, K. Zhao, Q. Ai, T. Terlier, L. Wang, L. Zhao, L. Guo, J. Lou, H. L. Xin, S. W. Martin and Y. Yao, *Nat. Commun.*, 2022, **13**, 2854.
16 A. Tron, *Solid State Sci.*, 2024, **153**, 107556.
17 S. Guo, Y. Su, K. Yan, C. Zhao, Y. Lu, H. Wang, J. Dong, N. Li, Y. Liu, Y. Guan, F. Wu and L. Chen, *Adv. Sci.*, 2024, 2404307.
18 M. Olson, S. Kmiec, N. Riley, N. Oldham, K. Krupp, A. Manthiram and S. W. Martin, *Inorg. Chem.*, 2024, **63**, 9129–9144.
19 Y. Zhu, E. R. Kennedy, B. Yasar, H. Paik, Y. Zhang, Z. D. Hood, M. Scott and J. L. M. Rupp, *Adv. Mater.*, 2024, **36**, 2302438.
20 S. W. Martin, *J. Am. Ceram. Soc.*, 1991, **74**, 1767–1784.
21 A. Kato, M. Yamamoto, A. Sakuda, A. Hayashi and M. Tatsumisago, *ACS Appl. Energy Mater.*, 2018, **1**, 1002–1007.

22 T. A. Yersak, Y. B. Zhang, F. Hao and M. Cai, *Front. Energy Res.*, 2022, **10**, DOI: 10.3389/fenrg.2022.882508.

23 S. Kmiec, M. Olson, M. Kenney and S. W. Martin, *Chem. Mater.*, 2022, **34**, 9479–9491.

24 M. Olson, S. Kmiec and S. W. Martin, *Inorg. Chem.*, 2022, **61**, 17469–17484.

25 R. Zhao, G. T. Hu, S. Kmiec, J. Wheaton, V. M. Torres and S. W. Martin, *Batteries Supercaps*, 2022, **5**, e202100356.

26 J. B. Bates, N. J. Dudney, B. Neudecker, A. Ueda and C. D. Evans, *Solid State Ionics*, 2000, **135**, 33–45.

27 S. Kalnaus, N. J. Dudney, A. S. Westover, E. Herbert and S. Hackney, *Science*, 2023, **381**, eabg5998.

28 S. Kalnaus, G. Yang, E. G. Herbert and A. S. Westover, *Mater. Today*, 2025, **86**, 580–587.

29 V. Torres III and S. W. Martin, *Inorg. Chem.*, 2023, **62**, 8271–8284.

30 N. J. Dudney, W. C. West and J. Nanda, *Handbook of Solid State Batteries*, World Scientific, 2015.

31 W. Yao and S. W. Martin, *Solid State Ionics*, 2008, **178**, 1777–1784.

32 N. Mascaraque, H. Takebe, G. Tricot, J. L. G. Fierro, A. Durán and F. Muñoz, *J. Non-Cryst. Solids*, 2014, **405**, 159–162.

33 W. Dai, Y. Qiao, Z. Ma, T. Wang and Z. Fu, *Future Mater.*, 2022, **1**, 032101.

34 N. Mascaraque, J. L. G. Fierro, F. Munoz, A. Duran, Y. Ito, Y. Hibi, R. Harada, A. Kato, A. Hayashi and M. Tatsumisago, *J. Mater. Res.*, 2015, **30**, 2940–2948.

35 F. Michel, F. Kuhl, M. Becker, J. Janek and A. Polity, *Phys. Status Solidi B*, 2019, **256**, 1900047.

36 R. Christensen, G. Olson and S. W. Martin, *J. Phys. Chem. B*, 2013, **117**, 16577–16586.

37 R. Shannon, *Acta Crystallogr. A*, 1976, **32**, 751–767.

38 G. Hu, V. M. Torres and S. W. Martin, *J. Non-Cryst. Solids*, 2023, **19**, 100198.

39 H. Es-soufi, L. Bih, B. Manoun and P. Lazor, *J. Non-Cryst. Solids*, 2017, **463**, 12–18.

40 M. A. Salorkar and V. K. Deshpande, *Phys. B*, 2022, **627**, 413590.

41 P. D. Mani, S. Saraf, V. Singh, M. Real-Robert, A. Vijayakumar, S. J. Duranceau, S. Seal and K. R. Coffey, *Solid State Ionics*, 2016, **287**, 48–59.

42 C. Dietrich, D. A. Weber, S. J. Sedlmaier, S. Indris, S. P. Culver, D. Walter, J. Janek and W. G. Zeier, *J. Mater. Chem. A*, 2017, **5**, 18111–18119.

43 R. Zhou, K. Luo, S. W. Martin and Q. An, *ACS Appl. Mater. Interfaces*, 2024, **16**, 18874–18887.

44 A. Kato, M. Nose, M. Yamamoto, A. Sakuda, A. Hayashi and M. Tatsumisago, *J. Ceram. Soc. Jpn.*, 2018, **126**, 719–727.

45 N. Aotani, K. Iwamoto, K. Takada and S. Kondo, *Solid State Ionics*, 1994, **68**, 35–39.

46 A. Hayashi, K. Minami, S. Ujiie and M. Tatsumisago, *J. Non-Cryst. Solids*, 2010, **356**, 2670–2673.

47 S. Kmiec, 27829602, PhD thesis, Iowa State University, 2020.

48 M. R. Busche, M. Weiss, T. Leichtweiss, C. Fiedler, T. Drossel, M. Geiss, A. Kronenberger, D. A. Weber and J. Janek, *Adv. Mater. Interfaces*, 2020, **7**, 2000380.

49 D. Y. Cheng, T. A. Wynn, X. F. Wang, S. Wang, M. H. Zhang, R. Shimizu, S. Bai, H. Nguyen, C. C. Fang, M. C. Kim, W. K. Li, B. Y. Lu, S. J. Kim and Y. S. Meng, *Joule*, 2020, **4**, 2484–2500.

50 N. Zhang, F. Ding, S. Yu, K. Zhu, H. Li, W. Zhang, X. Liu and Q. Xu, *ACS Appl. Mater. Interfaces*, 2019, **11**, 27897–27905.

51 X. Meng, Y. Xu, H. Cao, X. Lin, P. Ning, Y. Zhang, Y. G. Garcia and Z. Sun, *Green Energy Environ.*, 2020, **5**, 22–36.

52 B. Rowden and N. Garcia-Araez, *Energy Rep.*, 2021, **7**, 97–103.

53 O. L. Anderson and D. A. Stuart, *J. Am. Ceram. Soc.*, 1954, **37**, 573–580.

54 D. McElfresh and D. G. Howitt, *J. Am. Ceram. Soc.*, 1986, **69**, C238.

55 S. W. Martin, R. Christensen, G. Olson, J. Kieffer and W. Wang, *J. Phys. Chem. C*, 2019, **123**, 5853–5870.

56 R. Christensen, G. Olson and W. Martin Steve, *J. Phys. Chem. B*, 2013, **117**, 16577–16586.

57 S. Kmiec, M. Olson, M. Kenney and S. W. Martin, *Chem. Mater.*, 2022, **34**(21), 9479–9491.

58 S. W. Martin, R. Christensen, G. Olson, J. Kieffer and W. Wang, *J. Phys. Chem. C*, 2019, **123**, 5853–5870.